

Sequential Deep Learning Operator Network (S-DeepONet) for Time-Dependent Loads

Jaewan Park^{1,**}, Shashank Kushwaha^{1,**}, Junyan He^{1,**}, Seid Koric^{1,2*}, Diab Abueidda^{2,3}, Iwona Jasiuk¹

¹ *Department of Mechanical Science and Engineering, University of Illinois at Urbana-Champaign, Urbana, IL, USA*

² *National Center for Supercomputing Applications, University of Illinois at Urbana-Champaign, Urbana, IL, USA*

³ *Civil and Urban Engineering Department, New York University Abu Dhabi, Abu Dhabi, UAE*

Abstract

Deep Operator Network (DeepONet), a recently introduced deep learning operator network, approximates linear and nonlinear solution operators by taking parametric functions (infinite-dimensional objects) as inputs and mapping them to solution functions in contrast to classical neural networks (NNs) that need re-training for every new set of parametric inputs. In this work, we have extended the classical formulation of DeepONets by introducing recurrent neural networks (RNNs) in its branch in so-called sequential DeepONets (S-DeepONets) thus allowing accurate solution predictions in the entire domain for parametric and time-dependent loading histories. We have demonstrated this novel formulation's generality and exceptional accuracy with thermal and mechanical random loading histories applied to highly nonlinear thermal solidification and plastic deformation use cases. We show that once S-DeepONet is properly trained, it can accurately predict the final solutions in the entire domain and is several orders of magnitude more computationally efficient than the finite element method for arbitrary loading histories without additional training.

Keywords: Machine/Deep Learning, Recurrent Neural Netowrk (RNN), Deep Operator Network (DeepONet), Heat Transfer, Plastic Deformation

1. Introduction

Recent technological advances in high-performance computing hardware and machine learning (ML) methods have given rise to a wide range of applications in fields like autonomous driving, image and speech recognition, bioinformatics, medical diagnosis, document categorization, and others. Physics-based modeling has shown much interest in applications of Deep Learning with Artificial Neural Networks (ANN), a branch of machine learning motivated by the brain's biological structure and operation. Without the need for expensive computing power or modeling software, a well-trained surrogate deep learning model can almost immediately produce (infer) outcomes that are comparable with traditional modeling techniques. Many data-driven surrogate deep learning models have been devised and trained lately to quickly solve problems in additive manufacturing

*Corresponding author

Email address: koric@illinois.edu (Seid Koric^{1,2})

**The three authors contributed equally to this work

[1, 2], topologically optimized materials and structures [3–5], random heterogeneous materials [6], composite materials [7], nonlinear material responses [3, 8, 9], as well as a variety of other applications. Besides data-driven models, collocation point-based physics-informed neural networks (PINN) were created by Raissi et al. [10] and Abueidda et al. [11] capable of solving partial differential equations governing deformation and stress generation in solids or other physics without the aid of finite elements or other conventional numerical techniques, other than for validation. Similar to this, Nguyen-Thanh et al. [12], Samaniego et al. [13], Abueidda et al. [14, 15], Fuhg et al. [16] and He et al. [17, 18] devised a deep energy method (DEM), which makes use of potential energy to resolve nonlinear material responses. Besides forward problems, Haghighat et al. [19] used PINNs for inverse problems in solid mechanics. Cai et al. [20] even used a combination of measured data and a physics-informed deep-learning method to obtain a solution for an ill-posed thermal fluid flow that was previously thought to be unsolvable.

Nevertheless, most of these methods require retraining or transfer learning if input parameters like loads, boundary conditions, and material properties, or geometry change. The same is true of traditional numerical methods such as finite elements (FE) in that each new input parameter value calls for a new independent simulation. To address this problem, the universal approximation theorem for operators [21] inspired Lu et al.’s Deep Operator Network [22], often known as DeepONet, an innovative operator learning architecture. For a few linear and nonlinear PDEs in that landmark work, DeepONet successfully mapped between unknown parametric functions and solution spaces in addition to learning explicit operators like integrals. This gave rise to a powerful new method for solving stochastic and parametric PDEs. In the so-called physics-informed DeepONet, Wang et al. [23] improved the DeepONet formulation by including information from the governing PDE. They found improved prediction accuracy and data handling efficiency but at the expense of a higher computing cost for training. Recently, DeepONet has been used in heat conduction with a spatially variable heat source by Koric and Abueidda [24], fracture mechanics by Goswami et al. [25], and multiscale modeling using elastic and hyperelastic materials by Yin et al. [26], and elastic-plastic stress field prediction on topologically optimized geometries [27].

Many nonlinear thermal, mechanical, and multiphysics analyses have time-dependent loads often coupled with highly nonlinear thermo-mechanical properties, including phase transformation and/or materially nonlinear path-dependent constitutive models, such as in plastic deformation. Frequently, only the final stress or temperature field solution, obtained through incremental nonlinear finite element analysis, is of interest for analysis, designs, and optimizations. Such problems can be particularly computationally challenging and time-consuming for sensitivity analysis, uncertainty quantification, topological optimization, and similar iterative procedures where thousands, or even millions of forward evaluations, are needed to be done by classical nonlinear analysis to achieve statistical convergence. Koric et al. [28] used DeepONet for full-field stress prediction in plastic deformation with time-dependent loads and variable material properties using classical forward fully connected neural network (FNN) architecture in both branches of DeepONet. While the predictions were reasonably accurate in that work, the question was if advanced sequential learning methods, such as recurrent neural networks of the LSTM (Long short-term memory) and GRU (Gated recurrent unit) type, would provide universally and significantly more accurate full-field predictions by encoding random loading histories from various applications in the branch network of DeepONet. In this novel work, we have addressed that question.

This paper is organized as follows: Section 2 introduces three neural networks architectures and provides detail on the data generation method. Section 3 presents and discusses the performance of

the three models. Section 4 summarizes the outcomes and highlights future works.

2. Methods

2.1. Neural network models

This work explored three different NN architectures to predict the final temperature or von Mises stress distribution. All three NNs were implemented in the DeepXDE framework [29] with a TensorFlow backend [30].

2.1.1. FNN DeepONet

A DeepONet model with FNN in both the branch and trunk networks is used as the performance baseline. In an infinite-dimension functional input space M , $m \in M$ represents an input function with history-dependent load magnitudes defined on n control points (or input sensors) and refers to an unknown temperature or stress field solution in the functional solution space S . We consider that for every input $m \in M$ there is a solution $s = s(m) \in S$ for the temperature or stress field distribution from the Section 2.2.1 and Section 2.2.2, which are also subject to respective boundary conditions (BCs). Consequently, the mapping solution operator of a DeepONet $G : M \rightarrow S$ can be defined as:

$$G(m) = s(m). \quad (1)$$

For a collection of N points \mathbf{X} on a domain, each denoted by its coordinates (x_i, y_i) , the DeepONet considers both the load magnitudes m in its branch and positions \mathbf{X} in its trunk and predicts the solution operator $\hat{G}(m)(\mathbf{X})$ by combining intermediate encoded outputs b_i (from branch) and t_i (from trunk) in a dot product enhanced by bias β , as shown in a schematic of the FNN-based DeepONet model in Fig. 1. In a larger sense, it is possible to think of $\hat{G}(m)(\mathbf{X})$ as a function of \mathbf{X} conditioning on input m , and DeepONet is more general and capable than other neural networks. In both example cases, the time-dependent input load magnitude curves were discretized into $n = 101$

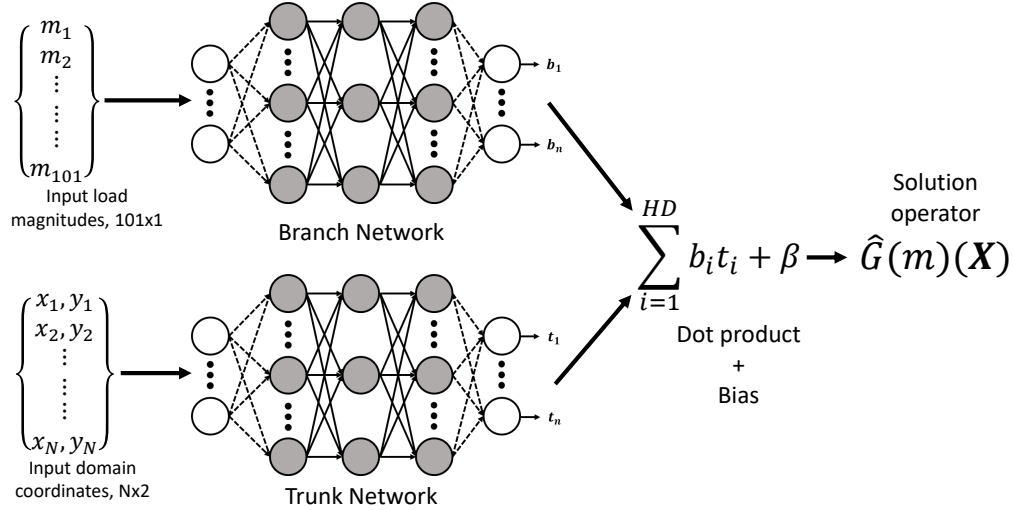


Figure 1: Schematic of the FNN-based DeepONet used in this work. m , x , y , b_i , t_i , HD , β and \hat{G} denote the load magnitude, X coordinate, Y coordinate, branch output, trunk output, hidden dimensions, the bias vector and the approximated solution operator.

time steps, and were fed into the branch FNN, which has seven layers (including input and output) with the following number of neurons: $[101, 100, 100, 100, 100, 100, HD]$. The trunk FNN network received the nodal coordinates of all nodes in the mesh, and has the following number of neurons: $[2, 100, 100, 100, 100, 100, HD]$. The output hidden dimension (HD) of both networks was set to 100, and the dot product operation combines the intermediate outputs of the two networks to produce the final output solution field. This network was applied to solve both problems introduced in Section 2.2. The total number of trainable parameters in the network is 111500. A larger network with similar number of parameters as in Section 2.1.2 was tested but showed similar performance as this smaller network, so the smaller network was used in the result sections. The model was trained for 351000 epochs with a batch size of 64. The Adam optimizer [31] was used and the scaled mean squared error (MSE) was used as the loss function.

2.1.2. S-DeepONet

The FNN-based DeepONet introduced in Section 2.1.1 uses a FNN to encode the time series signal of the input magnitude. However, time series signals are typically treated by RNNs [9, 32] due to their ability to capture causal relationship in the input signal, which significantly affects the final outcome for path-dependent problems like plasticity. However, in a FNN, the causality of the input data is not retained. The ability of RNNs to capture causality prompts us to apply RNNs in the branch to encode the time series signal. RNNs are referred to as recurrent because they carry out the same action for each element of a sequence, with the result depending on the results of earlier time-step calculations. RNN predicts the corresponding matching outputs for a given input sequence at each time step while minimizing the loss function between predictions and actual targets. Both encoder and decoder networks in Fig. 2 show an RNN cell symbolically being unfolded in time for an entire sequence. There is a hidden state at every time step, also known as the "memory" of the recurrent network, since it captures information about what happened in all the previous time steps. It is calculated from the previous hidden state and the input at the current step. Very deep computational graphs that continuously (recurrently) apply the same operation at each time step of a lengthy sequence are a common component of recurrent neural networks.

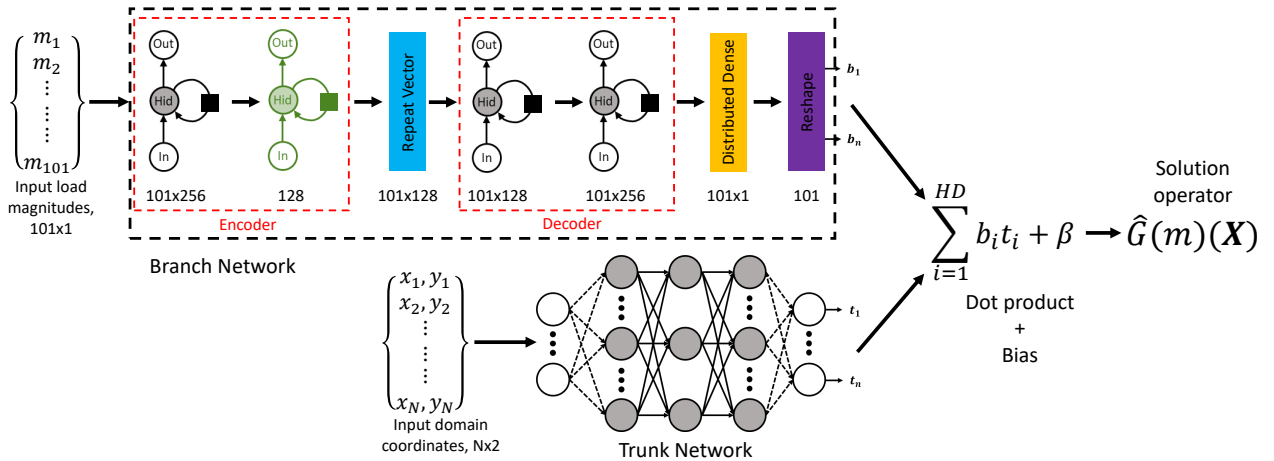


Figure 2: Schematic of the proposed S-DeepONet. The black RNN blocks returns a sequence (2D outputs), while the green RNN block does not return a sequence (1D output). m , x , y , b_i , t_i , HD , β and \hat{G} denote the load magnitude, X coordinate, Y coordinate, branch output, trunk output, hidden dimensions, the bias vector and the approximated solution operator.

It is difficult to train long sequence data with a simple RNN, which may result in vanishing or exploding gradient difficulties during backpropagation. Long short-term memory (LSTM) [33] and gated recurrent unit (GRU) [34] are solutions to the vanishing gradient issues of a simple RNN. In the LSTM and GRU advanced recurrent neural networks, hidden state (memory) cells are intended to dynamically "forget" some outdated and pointless information via particular gated units that regulate the information flow inside a memory cell, preventing the multiplication of a lengthy series of numbers during temporal backpropagation.

In this work, a branch network based on two different RNN layers, the LSTM and GRU, is proposed. Since the branch network of this novel DeepONet accepts sequence data, we named this architecture the S-DeepONet for short. An encoder-decoder structure is used in the branch, which was shown in many previous sequence-to-sequence prediction tasks to significantly improve the prediction accuracy [34–36]. In the context of DeepONet, the sequence-to-sequence mapping maps the loading history to a latent representation (the branch output), which is then merged with the latent representation of the domain geometry (the trunk output) via a dot product [29] to produce the final output prediction. Essentially, the proposed S-DeepONet aims to combine the powerful temporal encoding capability of the RNN structure in the branch with the spatial encoding capability of the DeepONet architecture. A schematic of the proposed S-DeepONet is shown in Fig. 2. The hidden dimension (HD) for the S-DeepONet is 101. The RNN blocks shown in Fig. 2 can be LSTM cells or GRU cells, leading to two different S-DeepONet models. The number of trainable parameters in the LSTM- and GRU-based S-DeepONet are 1038294 and 990358, respectively. Identical loss function and optimizer as mentioned in Section 2.1.1 were used to train the proposed two S-DeepONet models for a total of 351000 epochs.

2.2. Data generation

In this work, we demonstrate the application of the proposed S-DeepONets in transient heat transfer and structural deformation problems.

2.2.1. Transient heat transfer

In the first example, a nonlinear, transient heat transfer problem is studied, which is representative of a solidifying shell of low-carbon steel in a continuous caster [9]. Fig. 3 provides a schematic to illustrate the process.

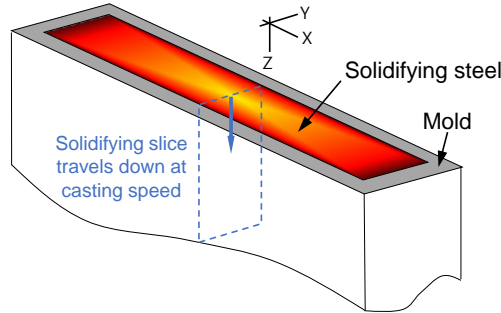


Figure 3: 3D schematic of molten steel solidifying in a caster mold.

To simplify the simulation, a 2D slice cross-section of the caster is modeled, which has a length of 30 mm and a width of 0.1 mm. As the domain moves down the mold in a Lagrangian frame

of reference, it is subject to a prescribed time-dependent heat flux extracting heat on one end, and all other surfaces are insulated. A schematic of the 2D problem domain is shown in Fig. 4. The

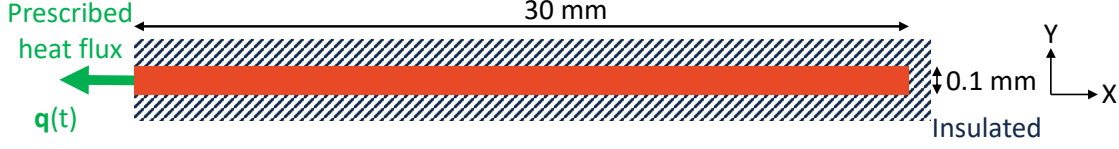


Figure 4: Schematic of the 2D domain used in the heat transfer problem.

governing equation and initial and boundary conditions of the transient heat transfer are given by:

$$\begin{aligned} \rho H(T) \frac{\partial T}{\partial t} &= \nabla \cdot [k(T) \nabla T], \\ -k(T) \nabla T &= \mathbf{q}(t), \quad \forall \mathbf{x} \in \partial\Omega_q, \\ T(x, 0) &= T_0, \end{aligned} \quad (2)$$

where t is time, T is temperature, ρ is mass density, and $\mathbf{q}(t)$ is the time-dependent heat flux. $T_0 = 1540$ °C is the uniform initial temperature. $H(T)$ and $k(T)$ denote the temperature-dependent specific enthalpy and isotropic thermal conductivity, respectively. It is highlighted that the specific enthalpy used in this work includes the latent heat effect during phase transformations, such as in solidification and transition from δ -ferrite to austenite, and brings significant nonlinearity to the system [37]. The material is a low carbon steel with a density of 7400 kg/m^3 ; other relevant material properties are shown in Table 1 and Table 2.

Table 1: Temperature-dependent material properties

Temperature [°C]	Conductivity [W/(m·K)]	Specific heat [J/(kg·K)]
800	28.934	695.44
1480.04	34.188	695.44
1519.73	39.000	824.61

Table 2: Latent heat properties

	Latent heat [J]	Liquidus temperature [°C]	Solidus temperature [°C]
Value	245100.0	1524.59	1475.43

The problem domain was discretized into 300 four-node bi-linear heat transfer elements (DC2D4) with an element size of 0.1 mm, and the thermal equation Eq. (2) is solved for a total of 17s that the slice spends in the caster traveling down the mold by using implicit time integration in Abaqus/Standard [37]. The temperature distribution at the end of the load step was extracted as the ground truth for NN training. To define a complex, time-dependent boundary heat flux, the sampling approach by Abueidda et al. [9] was used, where the time-dependent boundary heat flux is defined by six control points. The first and last control points ($_{cp}$) correspond to $t = 0$ and $t = 17s$, respectively. The time values (t_{cp}) for the four remaining control points were randomly sampled from a uniform distribution in range $(0, 17)s$. Based on experimental measurements, the flux value q_{cp} generally has a decaying profile and can be approximated as:

$$q_{cp} = A(t_{cp} + 1)^{-B} + C, \quad (3)$$

where $A \in [3, 8]$, $B \in [0.3, 0.7]$, and $C \in [-0.5, 0.5]$ were randomly chosen variables from their respective ranges. C can be considered as a random noise added to the flux magnitude to emulate additional fluctuations and nonlinearities observed in practice in the actual flux profile due to changes in contact and interfacial heat transfer between mold and steel [38, 39]. After all control points and the flux values are defined, a radial basis interpolation with Gaussian function is used to interpolate the flux. A total of 4000 cases were generated with distinct heat flux histories, and a typical example of the time-dependent heat flux is shown in Fig. 5a.

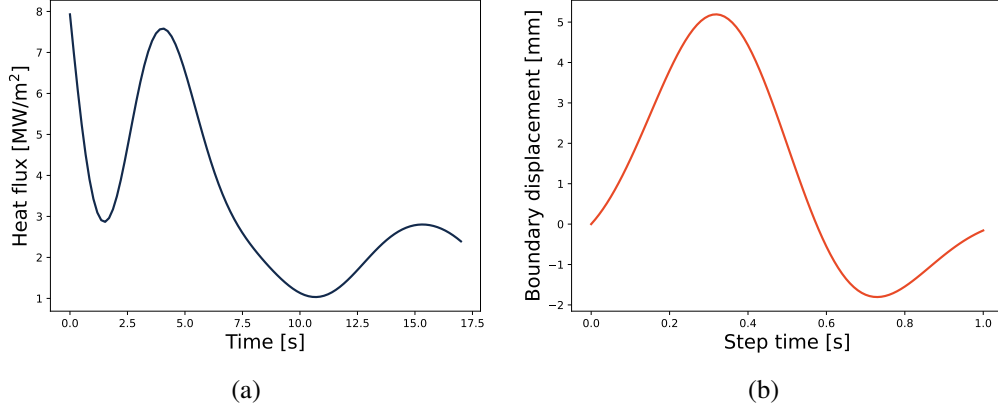


Figure 5: Typical time dependent load magnitudes: (a) Boundary heat flux in the transient heat transfer problem. (b) Applied displacement in the plastic deformation problem.

2.2.2. History-dependent plastic deformation

In the second example, plastic deformation of a dog bone specimen under a time-dependent loading history is studied, which follows from the recent work by Koric et al. [28]. The dog bone specimen has a length of 110 mm and a width (at the grip section) of 30 mm, with a gauge region width of 20 mm. A schematic of the domain along with the mesh used in FE simulations are shown in Fig. 6. A total of 4756 linear plane stress elements (four-node quadrilaterals and three-node triangles) were used to mesh the specimen with a plane-stress thickness of 1 mm. In the absence of any body and inertial forces, the equilibrium equations and boundary conditions can be stated in terms of the Cauchy stress σ as:

$$\begin{aligned} \nabla \cdot \sigma &= 0, \quad \forall \mathbf{X} \in \Omega, \\ \mathbf{u} &= \bar{\mathbf{u}}, \quad \forall \mathbf{X} \in \partial\Omega_u, \\ \sigma \cdot \mathbf{n} &= \bar{\mathbf{t}}, \quad \forall \mathbf{X} \in \partial\Omega_t, \end{aligned} \tag{4}$$

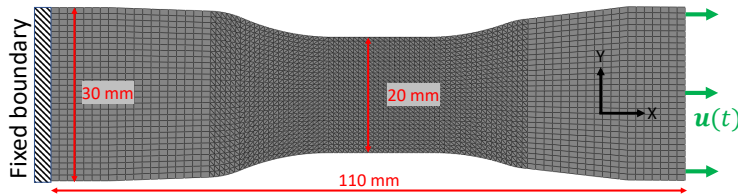


Figure 6: Schematic of the dogbone specimen and the mesh used in FE simulations. The applied displacement is along the global X axis.

where \mathbf{n} , $\bar{\mathbf{u}}$, and $\bar{\mathbf{t}}$ denote the outward boundary normal, prescribed displacement, and prescribed traction, respectively. Under small deformation assumption, total strain is given by:

$$\boldsymbol{\epsilon} = \frac{1}{2}(\nabla \mathbf{u} + \nabla \mathbf{u}^T), \quad (5)$$

The small-strain formulation of plasticity was used, so the total strain is decomposed additively into its elastic and plastic parts:

$$\boldsymbol{\epsilon} = \boldsymbol{\epsilon}^e + \boldsymbol{\epsilon}^p. \quad (6)$$

For linear elastic and isotropic material under plane stress condition, the constitutive equation is:

$$\begin{bmatrix} \sigma_{11} \\ \sigma_{22} \\ \sigma_{12} \end{bmatrix} = \begin{bmatrix} \frac{E}{1-\nu^2} & \frac{\nu E}{1-\nu^2} & 0 \\ \frac{\nu E}{1-\nu^2} & \frac{E}{1-\nu^2} & 0 \\ 0 & 0 & \frac{E}{2(1+\nu)} \end{bmatrix} \begin{bmatrix} \epsilon_{11} \\ \epsilon_{22} \\ \epsilon_{12} \end{bmatrix}, \quad (7)$$

where E and ν are the Young's modulus and Poisson's ratio. In this work, J_2 plasticity with linear isotropic hardening was used:

$$\sigma_y(\bar{\epsilon}_p) = \sigma_{y0} + H\bar{\epsilon}_p, \quad (8)$$

where σ_y , $\bar{\epsilon}_p$, σ_{y0} , and H denote the flow stress, equivalent plastic strain, initial yield stress, and the hardening modulus, respectively. The material properties of the elastic-plastic material response are presented in Table 3. The material model was integrated implicitly in Abaqus/Standard [37].

Table 3: Material properties of the elastic-plastic material model

Property	E [MPa]	ν [/]	σ_{y0} [MPa]	H [MPa]
Value	2.09×10^5	0.3	235	800

The specimen was fixed on the left side and a prescribed, time-dependent displacement was applied on the right edge. Six control points were used to define the loading path. Besides the two end points at $t = 0$ and $t = 1s$, four other control points were randomly sampled from the range $[0.1, 0.9]s$. The applied displacement is 0 at $t = 0$. The displacement magnitude at each control point was randomly selected such that the nominal axial strain magnitude is below 5%. Radial basis interpolation was used to interpolate the applied displacement at arbitrary time points. A typical example of the applied displacement is shown in Fig. 5b. A total of 4000 cases were generated, and the von Mises stress was stored as the ground truth labels in the NN training, and is defined as:

$$\bar{\sigma} = \sqrt{\sigma_{11}^2 + \sigma_{22}^2 + \sigma_{11}\sigma_{22} + 3\sigma_{12}^2}. \quad (9)$$

3. Results and discussion

FE simulations of the transient heat transfer and plastic deformation were conducted with eight high-end AMD EPYC 7763 Milan CPU cores. All NN training and inference were conducted using a single Nvidia A100 GPU card on Delta, an HPC cluster hosted at the National Center for Supercomputing Applications (NCSA). Of the 4000 data points for each problem, 3900 were used

in training the NNs, and 100 were used in testing. To evaluate the model performance in the test set, the relative L_2 error was used, which is given by:

$$\text{Mean } L_2 \text{ error} = \frac{1}{N_T} \sum_{i=1}^{N_T} \frac{|f_{FE} - f_{Pred}|_2}{|f_{FE}|_2}, \quad (10)$$

where N_T , f_{FE} , and f_{Pred} denote the total number of test cases, the FE-simulated field value, and the NN-predicted field value, respectively.

3.1. Transient heat transfer results

For the heat transfer problem, training of the FNN-, LSTM- and GRU-based DeepONet took 5486s, 20315s, and 18653s, respectively. The inference time for the three NN models compared to FE simulation time is shown in Table 4.

Table 4: Computational cost of the plastic deformation problem

	FE simulation time [s]	Inference time [s]	Speed up compared to FE (X)
FE simulation	60	/	/
FNN	/	5.13×10^{-3}	6.4×10^4
LSTM	/	2.24×10^{-2}	2.7×10^3
GRU	/	2.02×10^{-2}	3.0×10^3

Key statistics of the relative L_2 error on the test set for the three models are shown in Table 5. In an average sense, across all testing samples, both LSTM- and GRU-based DeepONet were able to lower the L_2 error of the FNN-DeepONet by half. To provide a better perspective of the error distribution over the 100 test cases, histograms of the error distribution are depicted in Fig. 7. To show the spatial distribution of the prediction error, selected cases are displayed in Fig. 8 with the final temperature distribution of the solidifying slice for the testing cases with the lowest, median, and largest L_2 errors, also dubbed as best, 50th percentile, and worst case. Line plots of the temperature at the center line of the domain as predicted by different DeepONet models are depicted in Fig. 9. It is observable that in the worst case, FNN in the branch fails to predict the temperature distribution correctly, particularly at the solidification front and the mushy zone, i.e., between Solidus and Liquidus temperatures. At the same time, LSTM and GRU in the branch provided an almost indistinguishable distribution from the target (FE simulation) temperature results for this case. Considering that the thickness of solidifying shell at the mold exit is calculated from the position of the solidifying front, in this case, the result inferred by classical DeepONet (with FNN in branch) will be of significantly less value for design, optimization, and online controls of this critical steel making process.

Table 5: Error statistics of three DeepONet models on the solidification heat transfer problem

	Mean	Std. deviation	Minimum	Maximum
FNN	0.0016	0.0025	0.0005	0.0201
LSTM	0.0005	0.0003	0.0002	0.0028
GRU	0.0006	0.0004	0.0003	0.0031

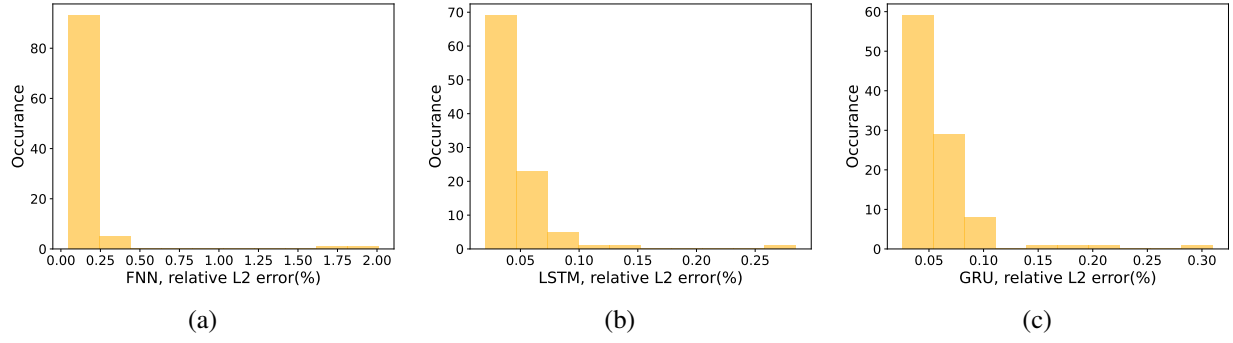


Figure 7: Histograms showing how the relative L_2 error distributes over the 100 test cases for the transient heat transfer case.

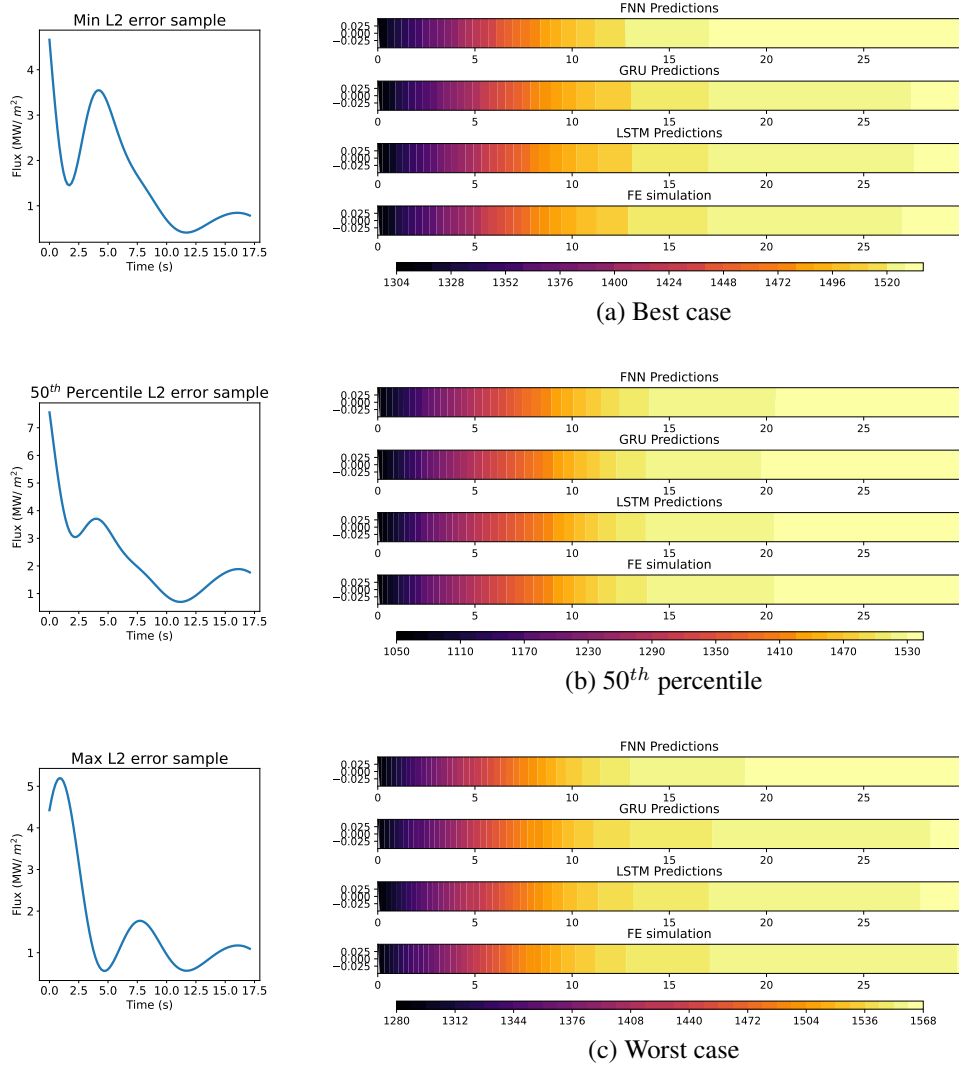


Figure 8: Comparison between FNN-, GRU- and LSTM-based DeepONets for the heat transfer example. Rows 1-3 correspond to the best, 50th percentile, and worst cases, respectively. The heat fluxes are shown in the first column.

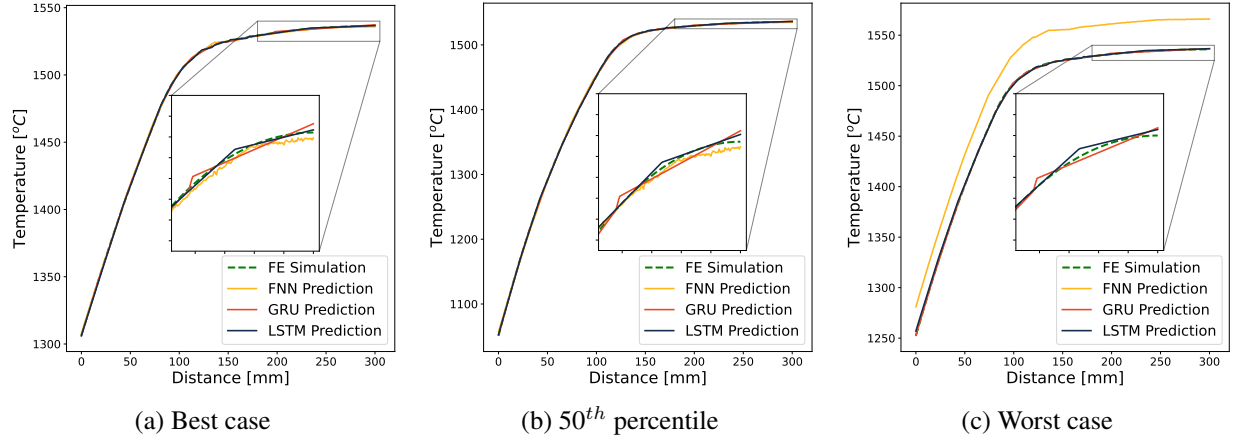


Figure 9: Line plots for the temperature distribution across the center line for different DeepONet models.

3.2. History-dependent plastic deformation results

For the plastic deformation problem, training of the FNN-, LSTM- and GRU-based DeepONet took 7805s, 20406s, and 18455s, respectively. The inference time for the three NN models compared to the FE simulation time is shown in Table 6. Key statistics of the relative L_2 error on the

Table 6: Computational cost of the plastic deformation problem

	FE simulation time [s]	Inference time [s]	Speed up compared to FE (X)
FE simulation	21	/	/
FNN	/	1.23×10^{-3}	1.7×10^4
LSTM	/	2.28×10^{-2}	9.2×10^2
GRU	/	2.06×10^{-2}	1.0×10^3

test set for the three models are shown in Table 7. To provide a better perspective of the error distribution over the 100 test cases, histograms of the error distribution are depicted in Fig. 10. To show the spatial distribution of the DeepONet prediction error, selected cases are displayed in Fig. 11. Line plots of the stress field along a downward diagonal line across the dogbone domain as predicted by different DeepONet models are depicted in Fig. 12.

Table 7: Error statistics of three DeepONet models on the plastic deformation problem

	Mean	Std. deviation	Minimum	Maximum
FNN	0.0288	0.0712	0.0019	0.4449
LSTM	0.0104	0.0237	0.0012	0.1281
GRU	0.0091	0.0200	0.0010	0.1325

The results in Fig. 11 and Fig. 12 indicate that the RNN-based S-DeepONets were able to predict the stress field significantly better than the regular FNN-based DeepONet in the worst-case scenario. In addition to the superior worst-case performance, on average, the S-DeepONets are twice as accurate compared to the FNN-based DeepONet, as seen in Table 7. These findings prove that the proposed S-DeepONet architecture effectively encodes complex, time-dependent loading

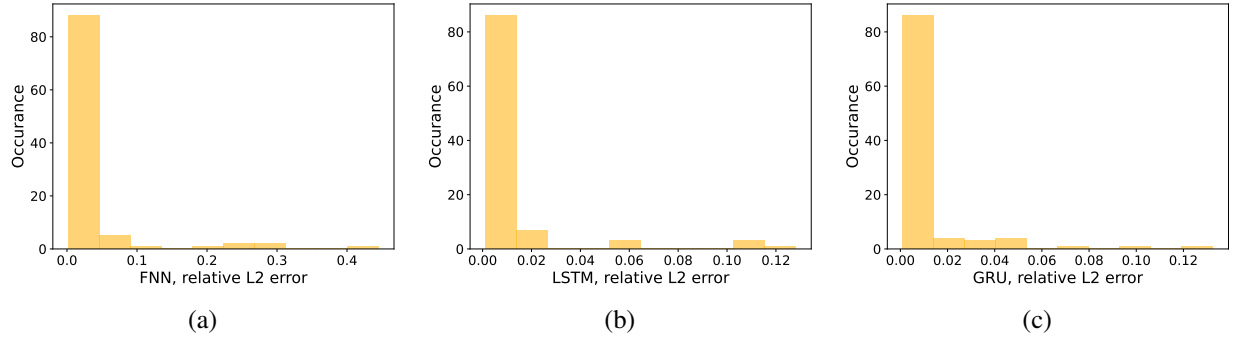


Figure 10: Histograms showing how the relative L_2 error distributes over the 100 test cases for the plastic deformation of the dog bone specimen.

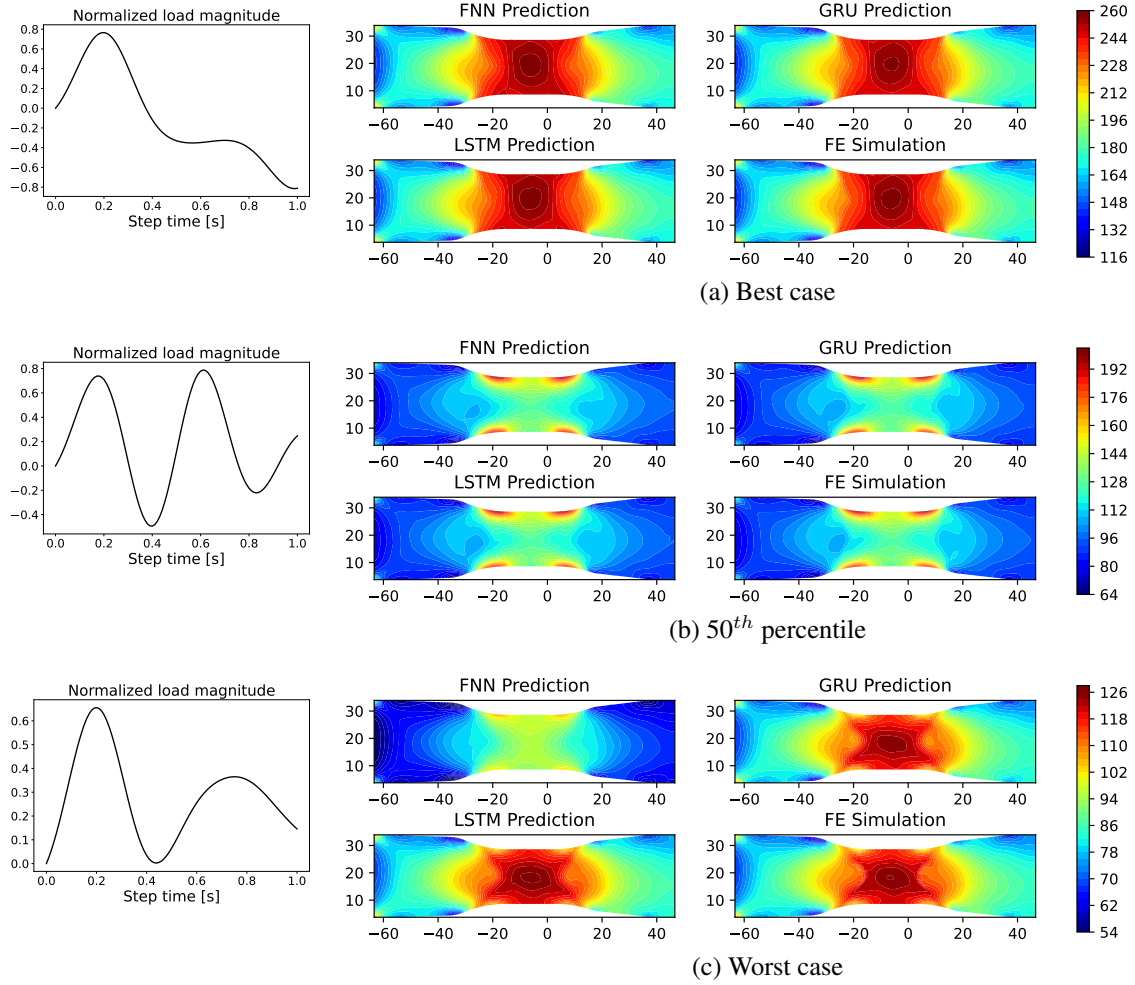


Figure 11: Comparison between FNN- and RNN-based DeepONet for the plastic deformation example. Rows 1-3 correspond to the best, 50th percentile, and worst cases, respectively. The normalized applied displacements are shown in the first column.

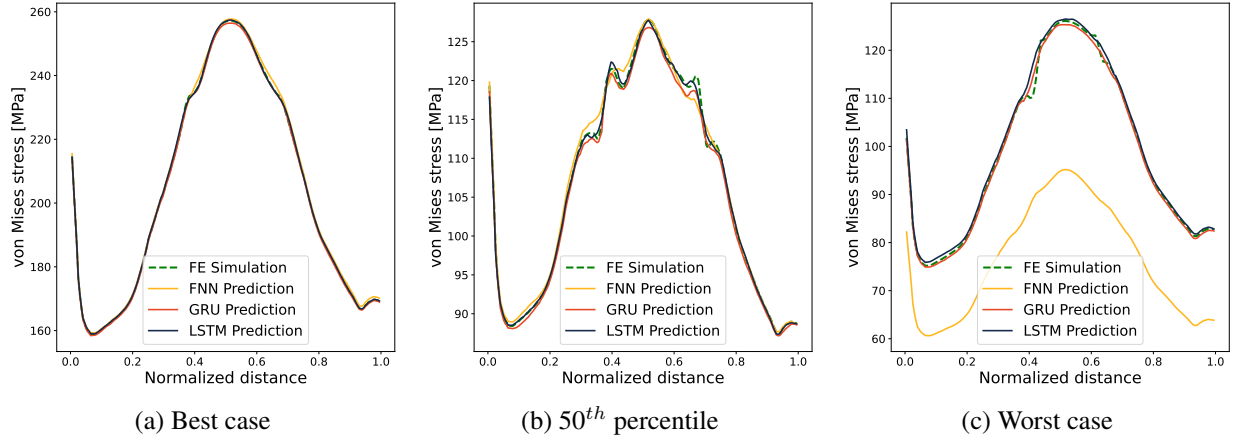


Figure 12: Line plots for the stress field across a downward diagonal line for different DeepONet models.

histories and performs better than the traditional FNN-based DeepONet. The spatial distribution of the predicted stress field closely resembles the FE ground truth, which indicates that the proposed S-DeepONets combines the temporal encoding capability of the RNN structure with the spatial encoding capability of the DeepONet architecture to improve prediction accuracy. However, it is worth noting that the training time of the RNN-based DeepONets were significantly longer than the FNN-based counterpart due to its more complex architecture and its recurrent nature. However, once the models were trained, the inference speed was several orders of magnitude faster than the FE simulation, which makes the S-DeepONet an attractive candidate where repeated function evaluation with different input loading histories are needed.

4. Conclusions and future work

After introducing the classical data-driven DeepONet framework, which leverages the fully connected neural networks (FNN) in the branch and trunk, we introduced the S-DeepONet, which we have formulated and devised with advanced, recurrent neural networks of LSTM and GRU types in the branch. We have then focused on learning full-field temperature and stress solutions in the two highly nonlinear practical applications of thermal and mechanical types with complex random loading histories. In both cases, S-DeepONet provided significantly more accurate predictions than classical DeepONet, proving that sequential learning methods in the branch of DeepONet can universally and effectively encode loading histories no matter the underlying physics of the problem. S-DeepONet was able to half the average error among all testing samples compared to DeepONet. The difference was even more profound for the worst testing sample, where S-DeepONet was able to correctly predict the temperature distribution in the solidification case and even recover stress concentration details in the plastic deformation of a dog bone specimen. We have shown that S-DeepONet can be adequately trained on the current high-end GPUs within a few hours. Moreover, once the S-DeepONet is properly trained, it can instantly infer accurate full-field results and several orders of magnitude faster than classical nonlinear numerical methods. Unlike classical DeepONet, which can provide instant full-field evaluations for preliminary design and optimizations, the increased accuracy of S-DeepONet may be robust enough to be used in full high-fidelity modeling, optimization, and design scenarios whenever a high number of forward evaluations with parametric

histories are needed in many complex nonlinear and non-equilibrium applications and processes in engineering and science. Furthermore, the trained S-DeepONet weights and biases can be transported to laptops and even edge computing devices and used for inference without the use of GPUs or even modeling tools for instant predictions in many online control scenarios. As the capabilities and memory of GPU hardware rapidly increase, in our future work, we will modify S-DeepONets for learning full solution fields from three-dimensional modeling domains.

Replication of results

The data and source code supporting this study’s findings can be made available to the corresponding author upon reasonable request.

Conflict of interest

The authors declare that they have no conflict of interest.

Acknowledgements

The authors would like to thank the National Center for Supercomputing Applications (NCSA) at the University of Illinois, and particularly its Research Computing Directorate, the Industry Program, and the Center for Artificial Intelligence Innovation (CAII) for their support and hardware resources. This research is a part of the Delta research computing project, which is supported by the National Science Foundation (award OCI 2005572) and the State of Illinois, as well as the Illinois Computes program supported by the University of Illinois Urbana-Champaign and the University of Illinois System. Finally, the authors would like to thank Professors George Karniadakis, Lu Lu, and the Crunch team at Brown, whose original work with DeepONets inspired this research.

CRedit author contributions

Jaewan Park: Methodology, Formal analysis, Investigation, Writing - Original Draft. **Shashank Kushwaha:** Methodology, Formal analysis, Investigation, Writing - Original Draft. **Junyan He:** Methodology, Formal analysis, Investigation, Writing - Original Draft. **Seid Koric:** Conceptualization, Methodology, Supervision, Resources, Writing - Original Draft, Funding Acquisition. **Diab Abueidda:** Supervision, Writing - Review & Editing. **Iwona Jasiuk:** Supervision, Writing - Review & Editing.

References

- [1] V Perumal, D Abueidda, S Koric, and A Kontsos. Temporal convolutional networks for data-driven thermal modeling of directed energy deposition. *Journal of Manufacturing Processes*, 85:405–416, 2023.
- [2] Ebrahim Sadeghpour and Aida Nonn. Data-driven models for structure-property prediction in additively manufactured steels. *Computational Materials Science*, 215:111782, 2022.
- [3] M Mozaffar, R Bostanabad, W Chen, K Ehmann, Jian Cao, and MA Bessa. Deep learning predicts path-dependent plasticity. *Proceedings of the National Academy of Sciences*, 116(52):26414–26420, 2019.
- [4] Hunter T Kollmann, Diab W Abueidda, Seid Koric, Erman Guleryuz, and Nahil A Sobh. Deep learning for topology optimization of 2d metamaterials. *Materials & Design*, 196:109098, 2020.
- [5] Junyan He, Charul Chadha, Shashank Kushwaha, Seid Koric, Diab Abueidda, and Iwona Jasiuk. Deep energy method in topology optimization applications. *Acta Mechanica*, 234(4):1365–1379, Apr 2023. ISSN 1619-6937. doi: 10.1007/s00707-022-03449-3. URL <https://doi.org/10.1007/s00707-022-03449-3>.

- [6] Enjamamul Hoq, Osama Aljarrah, Jun Li, Jing Bi, Alfa Heryudono, and Wenzhen Huang. Data-driven methods for stress field predictions in random heterogeneous materials. *Engineering Applications of Artificial Intelligence*, 123:106267, 2023.
- [7] Patrick Bleiziffer, Juergen Hofmann, Robert Zboray, Thorsten Wiege, and Roger Herger. Predicting the fiber orientation in glass fiber reinforced polymers using the moment of inertia and convolutional neural networks. *Engineering Applications of Artificial Intelligence*, 104:104351, 2021.
- [8] Franziska S Egli, Richard C Straube, André Mielke, and Tim Ricken. Surrogate modeling of a nonlinear, biphasic model of articular cartilage with artificial neural networks. *PAMM*, 21(1):e202100188, 2021.
- [9] Diab W Abueidda, Seid Koric, Nahil A Sobh, and Huseyin Sehitoglu. Deep learning for plasticity and thermo-viscoplasticity. *International Journal of Plasticity*, 136:102852, 2021.
- [10] Maziar Raissi, Paris Perdikaris, and George E Karniadakis. Physics-informed neural networks: A deep learning framework for solving forward and inverse problems involving nonlinear partial differential equations. *Journal of Computational physics*, 378:686–707, 2019.
- [11] Diab W Abueidda, Qiyue Lu, and Seid Koric. Meshless physics-informed deep learning method for three-dimensional solid mechanics. *International Journal for Numerical Methods in Engineering*, 122(23):7182–7201, 2021.
- [12] Vien Minh Nguyen-Thanh, Xiaoying Zhuang, and Timon Rabczuk. A deep energy method for finite deformation hyperelasticity. *European Journal of Mechanics-A/Solids*, 80:103874, 2020.
- [13] Esteban Samaniego, Cosmin Anitescu, Somdatta Goswami, Vien Minh Nguyen-Thanh, Hongwei Guo, Khader Hamdia, X Zhuang, and T Rabczuk. An energy approach to the solution of partial differential equations in computational mechanics via machine learning: Concepts, implementation and applications. *Computer Methods in Applied Mechanics and Engineering*, 362:112790, 2020.
- [14] Diab W Abueidda, Seid Koric, Rashid Abu Al-Rub, Corey M Parrott, Kai A James, and Nahil A Sobh. A deep learning energy method for hyperelasticity and viscoelasticity. *European Journal of Mechanics-A/Solids*, 95:104639, 2022.
- [15] Diab W Abueidda, Seid Koric, Erman Guleryuz, and Nahil A Sobh. Enhanced physics-informed neural networks for hyperelasticity. *International Journal for Numerical Methods in Engineering*, 124(7):1585–1601, 2023.
- [16] Jan N Fuhg and Nikolaos Bouklas. The mixed deep energy method for resolving concentration features in finite strain hyperelasticity. *Journal of Computational Physics*, 451:110839, 2022.
- [17] Junyan He, Diab Abueidda, Rashid Abu Al-Rub, Seid Koric, and Iwona Jasiuk. A deep learning energy-based method for classical elastoplasticity. *International Journal of Plasticity*, page 103531, 2023.
- [18] Junyan He, Diab Abueidda, Seid Koric, and Iwona Jasiuk. On the use of graph neural networks and shape-function-based gradient computation in the deep energy method. *International Journal for Numerical Methods in Engineering*, 124(4):864–879, 2023.
- [19] Ehsan Haghighat, Maziar Raissi, Adrian Moure, Hector Gomez, and Ruben Juanes. A physics-informed deep learning framework for inversion and surrogate modeling in solid mechanics. *Computer Methods in Applied Mechanics and Engineering*, 379:113741, 2021.
- [20] Shengze Cai, Zhicheng Wang, Frederik Fuest, Young Jin Jeon, Callum Gray, and George Em Karniadakis. Flow over an espresso cup: inferring 3-d velocity and pressure fields from tomographic background oriented schlieren via physics-informed neural networks. *Journal of Fluid Mechanics*, 915:A102, 2021.
- [21] Tianping Chen and Hong Chen. Universal approximation to nonlinear operators by neural networks with arbitrary activation functions and its application to dynamical systems. *IEEE Transactions on Neural Networks*, 6(4):911–917, 1995.
- [22] Lu Lu, Pengzhan Jin, Guofei Pang, Zhongqiang Zhang, and George Em Karniadakis. Learning nonlinear operators via deeponet based on the universal approximation theorem of operators. *Nature machine intelligence*, 3(3):218–229, 2021.
- [23] Sifan Wang, Hanwen Wang, and Paris Perdikaris. Learning the solution operator of parametric partial differential equations with physics-informed deeponets. *Science advances*, 7(40):eabi8605, 2021.
- [24] Seid Koric and Diab W Abueidda. Data-driven and physics-informed deep learning operators for solution of heat conduction equation with parametric heat source. *International Journal of Heat and Mass Transfer*, 203:123809, 2023.
- [25] Somdatta Goswami, Minglang Yin, Yue Yu, and George Em Karniadakis. A physics-informed variational deeponet for predicting crack path in quasi-brittle materials. *Computer Methods in Applied Mechanics and Engineering*, 391:114587, 2022.
- [26] Minglang Yin, Enrui Zhang, Yue Yu, and George Em Karniadakis. Interfacing finite elements with deep neural operators for fast multiscale modeling of mechanics problems. *Computer Methods in Applied Mechanics and Engineering*, 402:115027, 2022.
- [27] Junyan He, Seid Koric, Shashank Kushwaha, Jaewan Park, Diab Abueidda, and Iwona Jasiuk. Novel deeponet architecture to predict stresses in elastoplastic structures with variable complex geometries and loads. *arXiv preprint arXiv:2306.03645*, 2023.
- [28] Seid Koric, Asha Viswantah, Diab W Abueidda, Nahil A Sobh, and Kamran Khan. Deep learning operator network for plastic deformation with variable loads and material properties. *Engineering with Computers*, pages 1–13, 2023.
- [29] Lu Lu, Xuhui Meng, Zhiping Mao, and George Em Karniadakis. Deepxde: A deep learning library for solving differential equations. *SIAM review*, 63(1):208–228, 2021.
- [30] Martín Abadi, Ashish Agarwal, Paul Barham, Eugene Brevdo, Zhifeng Chen, Craig Citro, Greg S. Corrado, Andy Davis, Jeffrey Dean, Matthieu Devin, Sanjay Ghemawat, Ian Goodfellow, Andrew Harp, Geoffrey Irving, Michael Isard, Yangqing Jia, Rafal Jozefowicz, Lukasz Kaiser, Manjunath Kudlur, Josh Levenberg, Dandelion Mané, Rajat Monga, Sherry Moore, Derek Murray, Chris Olah, Mike Schuster, Jonathon Shlens, Benoit Steiner, Ilya Sutskever, Kunal Talwar, Paul Tucker, Vincent Vanhoucke, Vijay Vasudevan, Fernanda Viégas, Oriol Vinyals, Pete Warden, Martin Wattenberg, Martin Wicke, Yuan Yu, and Xiaoqiang Zheng. TensorFlow: Large-scale machine learning on heterogeneous systems, 2015. URL <https://www.tensorflow.org/>. Software available from tensorflow.org.
- [31] Diederik P Kingma and Jimmy Ba. Adam: A method for stochastic optimization. *arXiv preprint arXiv:1412.6980*, 2014.
- [32] Junyan He, Shashank Kushwaha, Diab Abueidda, and Iwona Jasiuk. Exploring the structure-property relations of thin-walled, 2d extruded lattices using neural networks. *Computers & Structures*, 277:106940, 2023.
- [33] Jürgen Schmidhuber, Sepp Hochreiter, et al. Long short-term memory. *Neural Comput*, 9(8):1735–1780, 1997.
- [34] Kyunghyun Cho, Bart Van Merriënboer, Caglar Gulcehre, Dzmitry Bahdanau, Fethi Bougares, Holger Schwenk, and Yoshua Bengio. Learning phrase representations using rnn encoder-decoder for statistical machine translation. *arXiv preprint arXiv:1406.1078*, 2014.
- [35] Pankaj Malhotra, Anusha Ramakrishnan, Gaurangi Anand, Lovekesh Vig, Puneet Agarwal, and Gautam Shroff. Lstm-based encoder-decoder for multi-sensor anomaly detection. *arXiv preprint arXiv:1607.00148*, 2016.
- [36] Ilya Sutskever, Oriol Vinyals, and Quoc V Le. Sequence to sequence learning with neural networks. *Advances in neural information processing systems*, 27, 2014.
- [37] SIMULIA. Abaqus, 2020.

- [38] Matthew LS Zappulla, Seong-Mook Cho, Seid Koric, Hyoung-Jun Lee, Seon-Hyo Kim, and Brian G Thomas. Multiphysics modeling of continuous casting of stainless steel. *Journal of Materials Processing Technology*, 278:116469, 2020.
- [39] Seid Koric and Brian G Thomas. Efficient thermo-mechanical model for solidification processes. *International journal for numerical methods in engineering*, 66(12):1955–1989, 2006.